# Behaviour of lightweight aggregate concrete-filled steel tube under horizontal cyclic load

Zhongqiu Fu [a], Bohai Ji*, Dongyang Wu [b] and Zhenpeng Yu [c]

*College of Civil and Transportation Engineering, Hohai University, No.1 Xikang Road, Nanjing, China*

**Abstract.**   A horizontal cyclic test was carried out to study the seismic performance of lightweight aggregate concrete filled steel tube (LACFST). The constitutive and hysteretic model of core lightweight aggregate concrete (LAC) was proposed for finite element simulation. The stress and strain changes of the steel tube and concrete filled inside were measured in the experiment, and the failure mode, hysteresis curve, skeleton curve, and strain curve of the test specimens were obtained. The influence of axial compression ratio, diameter-thickness ratio and material strength were analysed based on finite element model. The results show that the hysteresis curve of LACFST indicated favourable ductility, energy dissipation, and seismic performance. The LACFST failed when the concrete in the bottom first crushed and the steel tube then bulged, thus axial force imposed by prestressing was proved to be feasible. The proposed constitutive model and hysteretic model of LAC under the constraint of its steel tube was reliable. The bearing capacity and ductility of the specimen increase significantly with increasing thickness of the steel tube. The bearing capacity of the member improves while the ductility and energy dissipation performance slightly decreased with the increasing strength of the steel and concrete.

**Keywords:**   lightweight aggregate concrete filled steel tube; horizontal cyclic test; hysteretic behaviour; concrete constitutive model

## 1. Introduction

Concrete filled steel tubes (CFST) have been widely applied in civil engineering because of their high bearing capacity, good seismic performance, and convenience in construction (Roeder *et al*. 2018, Krishan *et al*. 2016). The self-weight can be reduced without weakening its strength if lightweight aggregate concrete is applied to fill the steel tube (Fu *et al*. 2018), which can be better adapted to the development of modern materials with light weight and high strength. It has been shown that lightweight aggregate concrete filled steel tubes (LACFST) have superior mechanical performance than the same steel tube filled with ordinary concrete (Yu *et al*. 2016) and can be applied for engineering use in high-rise and large-span structures. The basic static performance of LACFST (Ji *et al*. 2013) has been studied while the seismic performance under horizontal cyclic load has not assessed. Many scholars have studied the seismic performance of CFST columns; however, the study of CFST under static load shows that CFST and LACFST vary a lot in the restraint of the steel tube and failure of the core concrete, which leads to different bearing performances including that under seismic load.

It has been found in the quasi-static test that the ordinary CFST exhibits good bearing capacity and ductility under horizontal cyclic load (Ge and Usami 1996, Inai *et al*. 2004, Arivalagan and Kandasamy 2010). Many scholars have analysed previous experimental research and proposed a numerical calculation method for quasi-static analysis of ordinary CFST, which has been verified experimentally (Hajjar 2000, Skalomenos *et al*. 2015, Duarte *et al*. 2016). However, due to the differences between lightweight aggregate concrete materials, these calculation methods cannot simulate the hysteretic changes in LACFST. In particular, advanced testing equipment is required for application of the axial force, and failure loads of the core concrete are rarely tested. In recent years, the study of the seismic behaviour of CFST focused on high-strength steel pipes (Varma *et al*. 2000), joint nodes (Lee *et al*. 2015, Khanouki *et al*. 2016, Esfandyary *et al*. 2015), and new concrete-filled structures (Subramoni *et al*. 2018, Kim *et al*. 2015). The research into the mechanical behaviour of LACFST under horizontal cyclic load has not yet been carried out. The failure mode of LACFST is mainly analysed by the broken state of the specimens (Ghannam *et al*. 2004) while the failure mode and the interaction between the steel pipe and the core concrete have not been comprehensively studied.

Here, the axial force of the specimen was applied by tensioning the prestressed steel cables and different axial compression ratio parameters could be achieved. A thin copper plate with a strain gauge was buried in the specified position and the conductor was removed to test the core concrete during construction. The testing of several

---

∗Corresponding author, Professor,
 E-mail: bhji@hhu.edu.cn
[a] Ph.D., E-mail: fuzhongqiu@hhu.edu.cn
[b] Master Student, E-mail: 1067161021@qq.com
[c] Master Student, E-mail: 1290665224@qq.com

specimens under horizontal cyclic load was carried out and the modified constitutive model of concrete was simulated. The seismic performance of LACFST was studied based on bearing capacity, energy dissipation, and failure mode.

## 2. Experimental procedures

### 2.1 Design and production of test specimens

The welded steel tube used in the test is round and straight and made of Q235 steel. According to Chinese Standard "Metallic materials at ambient temperature: tensile test method" (GB/T228-2002) (2002), the tensile strength, elastic modulus, and Poisson's ratio of the steel obtained by standard tensile test are 260 MPa, 205,000 MPa, and 0.276 respectively. The concrete used in the test is lightweight aggregate concrete (a CL30 mix: see Table 1), wherein the coarse aggregate particle size ranges from 1 to 3 mm; the fine aggregate is medium coarse sand with a fineness modulus of 2.8 and an apparent density of 2700 kg/m³; PC 32.5 composite Portland cement is used; and the water is ordinary tap water. Three sets of light aggregate concrete cube test blocks were made separately, and the cubic compressive strength test was carried out by LS compression test machine to obtain the cube compressive strength ($f_{cu}$) and elastic modulus ($E_c$) of the light aggregate concrete, which were 31.35 MPa and 2.39 × 10⁴ MPa, respectively.

Two sets of eight test specimens were designed and fabricated, respectively. The axial compression ratio ($n$) of 0, 0.1, and 0.2 was considered in each set of tests. A hole with a diameter of 16 mm was reserved at the centre of the upper and lower ends of the steel tube during concrete pouring. The PVC pipe was pre-buried in the tunnel, and the axial force was applied by tensioning the pre-stressed steel cables. At the same time, a non-porous test piece was designed and manufactured to compare and analyse the

influence of the pre-stressed steel pipe on the test piece. The specific parameters of each test piece are shown in Table 2. In Table 2, $D$ is the external diameter, $t$ is the thickness, $L$ is the length of the steel. $n$ is the axial compression ratio.

The horizontal cyclic loading on the test piece was applied by hydraulically actuating the head. To prevent local buckling of the base plate of the test piece during the test, a concrete block with a height of 70 mm was placed between the test piece bottom plate and the concrete ground anchor. The rod connected the test piece, the concrete block, and the ground anchor. The horizontal loading of the test piece and the axial prestressed steel bar loading diagram are shown in Figs.1 and 2.

### 2.2 Measuring point arrangement

Strain gauges were arranged in three sections of specimens. The layout sections were named A-20, A-80, and A-180, i.e., the distance from the bottom of the test piece was 20 mm, 80 mm, and 180 mm, respectively. A triaxial strain gauge and three uniaxial strain gages were arranged in each section, wherein the triaxial strain gauges
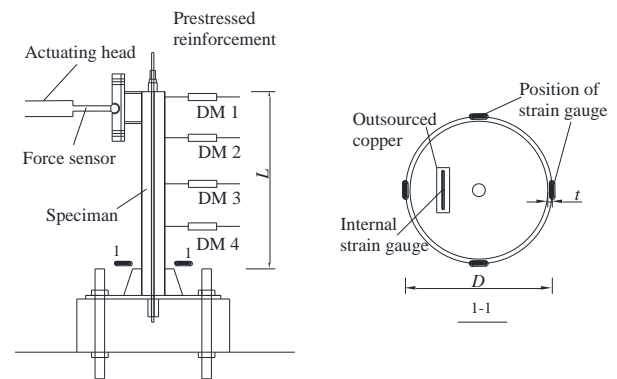


Fig. 1 Test loading and stain gauge arrangement

Table 1 Light aggregate concrete material parameters

| Cement (kg/m³) | Ceramsite (kg/m³) | Sand (kg/m³) | Water (kg/m³) | $f_{cu}$ (MPa) | $E_c$ (MPa) | Poisson's ratio |
|---|---|---|---|---|---|---|
| 18.40 | 26.80 | 26.00 | 11.60 | 31.35 | 2.39 × 10⁴ | 0.17 |

Table 2 Parameters of the specimens

| Specimens | Tube sizes (mm) | | | Hoop coefficient $\xi$ | $n$ | Axial load $N$ (kN) | Remarks |
|---|---|---|---|---|---|---|---|
| | $D$ (mm) | $L$ (mm) | $t$ (mm) | | | | |
| CFST-A-1 | 114 | 1000 | 3 | 0.86 | 0 | 0 | No hole |
| CFST-A-2 | 114 | 1000 | 3 | 0.86 | 0.1 | 52 | With holes |
| CFST-A-3 | 114 | 1000 | 3 | 0.86 | 0.2 | 104 | With holes |
| CFST-A-4 | 114 | 1000 | 3 | 0.86 | 0 | 0 | With holes |
| CFST-B-1 | 133 | 1000 | 3 | 1.17 | 0 | 0 | No hole |
| CFST-B-2 | 133 | 1000 | 3 | 1.17 | 0.1 | 67 | With holes |
| CFST-B-3 | 133 | 1000 | 3 | 1.17 | 0.2 | 134 | With holes |
| CFST-B-4 | 133 | 1000 | 3 | 1.17 | 0 | 0 | With holes |

Fig. 2 Test under load



Fig. 3 Displacement-controlled loading
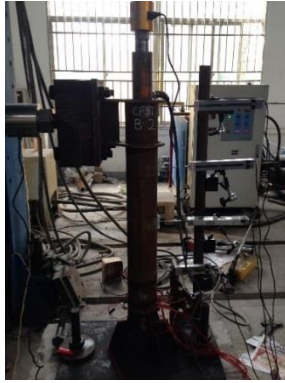
were arranged in the direction of action of the hydraulic actuator, and the uniaxial strain gauges were respectively arranged on three tangent planes symmetrically. The triaxial strain gauges on section A-20 were numbered from 1 to 3 which corresponded to the direction of the strain gauges (0°, 45°, and 90°), respectively. The uniaxial strain gauges were numbered from 4 to 6 clockwise. The uniaxial strain gauges on sections A-80 and A-180 were numbered from 7 to 12 and 13 to 18. In addition, a uniaxial strain gauge was attached to sections A-20, A-80, and A-180 by thin copper plate, which was embedded into concrete during construction. The internal strain gauges in sections A-20 to A-180 were numbered 19, 20, and 21. The layout of strain gauges inside the concrete is shown in Fig. 2.

Four displacement meters were placed along the height of the specimens to measure the horizontal displacement of each section during the loading process. The distance between the displacement meter and the top of the specimen was 20 mm, 250 mm, 500 mm, and 750 mm (DM1, DM2, DM3, and DM4), respectively. The measuring range of DM1, DM2, and DM3 was from -100 mm to +100 mm, and that of DM4 was from 50 mm to +50 mm.

### 2.3 Loading system

The loading process contained three steps for force-controlled to displacement-controlled, then force-displacement controlled again. Force-controlled loading was for the steps of contacting and failure. Displacement-controlled method was accepted for the main test loading step. The bearing capacity, displacement and seismic response of the specimens were observed. The loading was carried out before, and after, the yield of each specimen, respectively. The loading before the yield was applied in one cycle, and the loading displacement was 4, 8, 12, 4 + 4$n$ and so on ($n$ was the number of cycles). The specimen was assumed to yield if the displacement increased with no change of the loading. The loading ended before yield. The loading (post-yield) was applied over three cycles, and the loading displacement was 2$\Delta y$, 3$\Delta y$, and 4$\Delta y$ ($\Delta y$ was the yield displacement). The specimen was assumed to fail if the horizontal load was reduced to 85% of the maximum load, so the loading was stopped. The loading cycle was 4 min and the loading system is shown in Fig. 3.
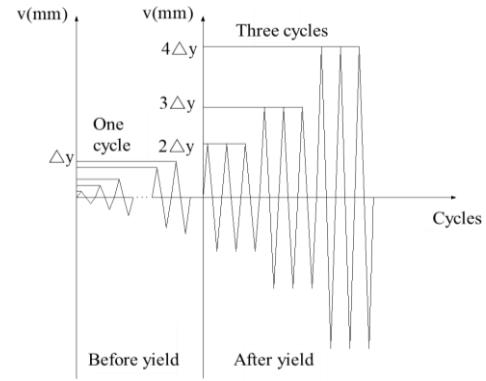
## 3. Analysis model

### 3.1 Material constitutive

The non-linear follow-up strengthening model was used for the steel. The Bauschinger effects in steel, which can simulate the mechanical behaviour under horizontal cyclic load, were considered. The deformation was resisted by the elastic stiffness before the specimen yielded. Then the modulus of the steel during the hardening stage was taken as $0.01E_s$, the elastic modulus and Poisson's ratio of the steel were 206,000 MPa and 0.283, respectively (Liu 2013).

The plastic damage model was adopted for CFST, which considered the behaviour of concrete material damage, crack development, crack closure and stiffness recovery under cyclic load. The compressive stress-strain curve of the plastic damage model consisted of ascending and descending sections. The concrete stress-strain curve proposed by Samani and Attard (2012) was applied for the ascending section. The curve was modified considering different compressive performance between the CFST and ordinary concrete aggregate.

$$\frac{\sigma}{f'_{cc}} = \frac{A \cdot x + B \cdot x^2}{1 + (A-2)x + (B-1)x^2} \tag{1}$$

Where, $x = \varepsilon/\varepsilon_{c0}$, in which $\varepsilon_{c0}$ is the strain corresponding to peak stress under compression; $f'_{cc} = f_c'^{1.02}\left(0.9 + 0.34e^{-\xi/1.63}\right)$, in which $f_c'$ is the compressive strength of cylinder; $A = E_c\varepsilon_{c0}/f'_{cc}$ ; $B = (A-1)^2/0.55 - 1$.

The formula suggested by Guo (1982) was adopted for the descending section

$$y = \frac{x}{\alpha(x-1)^2 + x} \tag{2}$$

$\alpha$ affects the slope of the falling section which mainly depends on the strength of the concrete and the coefficient of confinement effect $\xi$. As the confinement effect $\xi$ could be expressed by $\xi = \frac{A_s f_y}{A_c f_{c'}}$, thus $\alpha = \frac{f_c'^{0.16}}{10(1-e^{-\xi/0.63})}$.

The damage factor $d_{c(t)}$ was calculated according to the "focal method" proposed by Liu (2013).

$$d_{c(t)} = 1 - \frac{\sigma_{c(t)} + n_{c(t)}\sigma_{c0(t0)}}{E_{oc(0t)}\left(n_{c(t)}\sigma_{c0(t0)}/E_{0c(0t)} + \varepsilon_{c(t)}\right)} \quad (3)$$

Where, $\sigma_{c(t)}$ is the compressive (tensile) stress; $\varepsilon_{c(t)}$ is the compressive (tensile) strain; $\sigma_{c0(t0)}$ is the compressive (tensile) peak stress on the concrete; $E_{c0(t0)}$ is the initial compressive (tensile) elastic modulus of concrete.

### 3.2 Finite element model

The FE model sizes were the same with the specimens. The meshing procedure was formed by sweeping. The circumference steel tube was divided into 20 elements and the size was 17 mm. The four-node reduced integration shell element (S4R) was adopted for the steel tube. Simpson integration (nine points used) was applied along the thickness of the shell element to meet the required calculation accuracy. The three-dimensional solid element (C3D8R) was applied for the core concrete and the loading plate. The interface between the steel pipe and the CFST consisted of two parts: contact in the normal direction and bond slip in the tangential direction. The contact line in the tangential direction was a penalty function. The friction coefficient between the steel pipe and the concrete was 0.6 (Liu 2013). The contact in the normal direction was a hard contact, that is, the pressure perpendicular to the contact surface can be transmitted between the interfaces. The contact element was a surface-to-surface contact in which the steel shell element was the main surface and the concrete solid unit was the secondary surface. One end of the member was a fixed end, and Reference Point 1 was set outside the other end of the member. Coupling Reference Point 1 and the upper part of the member, a horizontal reset displacement load was applied to Reference Point 1. The loading system and specimen size were consistent with the test (Figs. 2 and 3).

### 3.3 Hysteretic model

It could be observed that the LACFST experienced three stages of behaviour under the horizontal cyclic load, namely the strain-elasticity stage, the strain-plasticity stage, and the strain-softening stage, which agrees well with the trilinear linear model (Fig. 4). The hysteretic model of the LACFST under the horizontal cyclic load was proposed based on a previous study by Han and Yang (2005) who derived a P-Δ
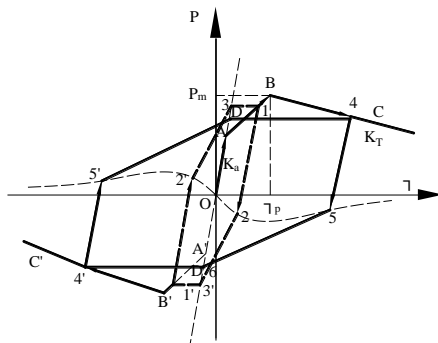


Fig. 4 The hysteretic model

model for an ordinary CFST.

The hysteretic model of CFST with circular steel tube was shown in Fig. 4. Point A illustrated the end of the strain-elasticity stage. The lateral load $P$ was 0.6 times of the peak load $P_m$ and the rigidity of OA was $K_a$. Point B denoted the peak of the hysteretic model. The lateral load was $P_m$ which corresponded to the displacement $\Delta_p$. The values of those parameters mentioned above were as follows

$$K_a = 3K_e/2L^3 \quad (4)$$

Where, $K_e = E_sI_s + 0.6E_cI_c$; $E_S$ and $E_C$ denoted the elasticity of the steel and concrete; and $I_S$ and $I_c$ denoted the section moment of inertia of the steel tube and concrete body.

The displacement $\Delta_p$ of Point B was influenced by the yield strength $f_y$ of steel, the slenderness ratio $\lambda$, and axial pressure ratio $n$. It was given by

$$\Delta_p = \frac{6.74 \cdot [(\ln r)^2 - 1.08 \cdot \ln r + 3.33] \cdot f_1(n)}{(8.7 - f_y/345)} \cdot \frac{P_m}{K_a} \quad (5)$$

Where, $r = \lambda/40$;
$$f_1(n) = \begin{cases} 1.336 \cdot n^2 - 0.044 \cdot n + 0.804 & (0 \le n \le 0.5) \\ 1.126 - 0.02 \cdot n & (0.5 < n < 1) \end{cases}$$

The lateral load $P_m$ was mainly influenced by the slenderness ratio $\lambda$ and hoop coefficient $\xi$:

$$P_m = \begin{cases} (0.95 \cdot \alpha - 0.2n) \cdot \dfrac{M_y}{L_1} & (1 \le \xi \le 4) \\ \alpha \cdot (0.2 \cdot \xi + 0.65 - 0.14n) \cdot \dfrac{M_y}{L_1} & (0.2 \le \xi \le 1) \end{cases} \quad (6)$$

Where $\alpha =$
$$\begin{cases} 0.96 - 0.002 \cdot \xi & (0 \le n \le 0.3) \\ (1.4 - 0.34 \cdot \xi) \cdot n + 0.1 \cdot \xi + 0.54 & (0.3 \le n \le 1) \end{cases} \cdot M_y$$
denoted the bending capacity of the LACFST as proposed by Fu (2018) and could be given by ($\gamma_m = 1.1$)

$$M_y = 0.17 \cdot \gamma_m D(1 + \xi)f_{ck}A_c \quad (7)$$

The rigidity $K_T$ of line BC could be calculated by Eq. (8).

$$K_T = \frac{0.03 \cdot f_2(n) \cdot f(r, \alpha) \cdot K_a}{(c^2 - 3.39 \cdot c + 5.41)} \quad (8)$$

Where, $\gamma_m$ is an enhancement coefficient considering the contribution of steel after yielded. Here, $\gamma_m = 1.0$. $c = f_{cu}/60$ $f_{ck}$ was the compressive strength of prism and $f_{cu}$ was the compressive strength of cube. The concrete strength of prism, cube and cylinder can be converted between each other according to empirical formula. Other means were as following.

$$f_2(n) = \begin{cases} -5.1 \cdot n - 1.2 & (0 \le n \le 0.7) \\ 0.5 \cdot n + 1.57 & (0.7 < n < 1) \end{cases} \quad (9)$$

$$f(r, \alpha) = \begin{cases} (8 \cdot \alpha - 8.6) \cdot r + 6 \cdot \alpha + 0.9 & (r \le 1) \\ (15 \cdot \alpha - 13.8) \cdot r + 6.1 - \alpha & (r > 1) \end{cases} \quad (10)$$
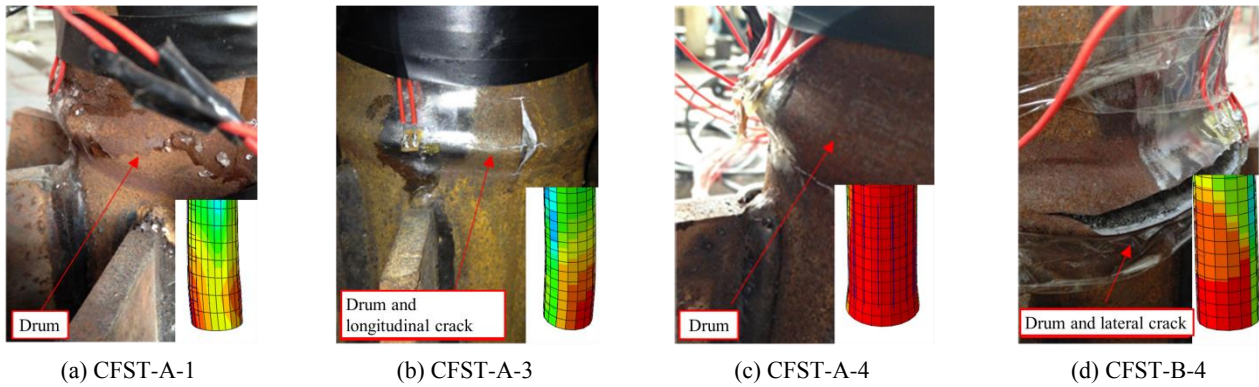
(a) CFST-A-1      (b) CFST-A-3      (c) CFST-A-4      (d) CFST-B-4

Fig. 5 Form of destruction



(a) CFST-A-1      (b) CFST-A-2      (c) CFST-A-4

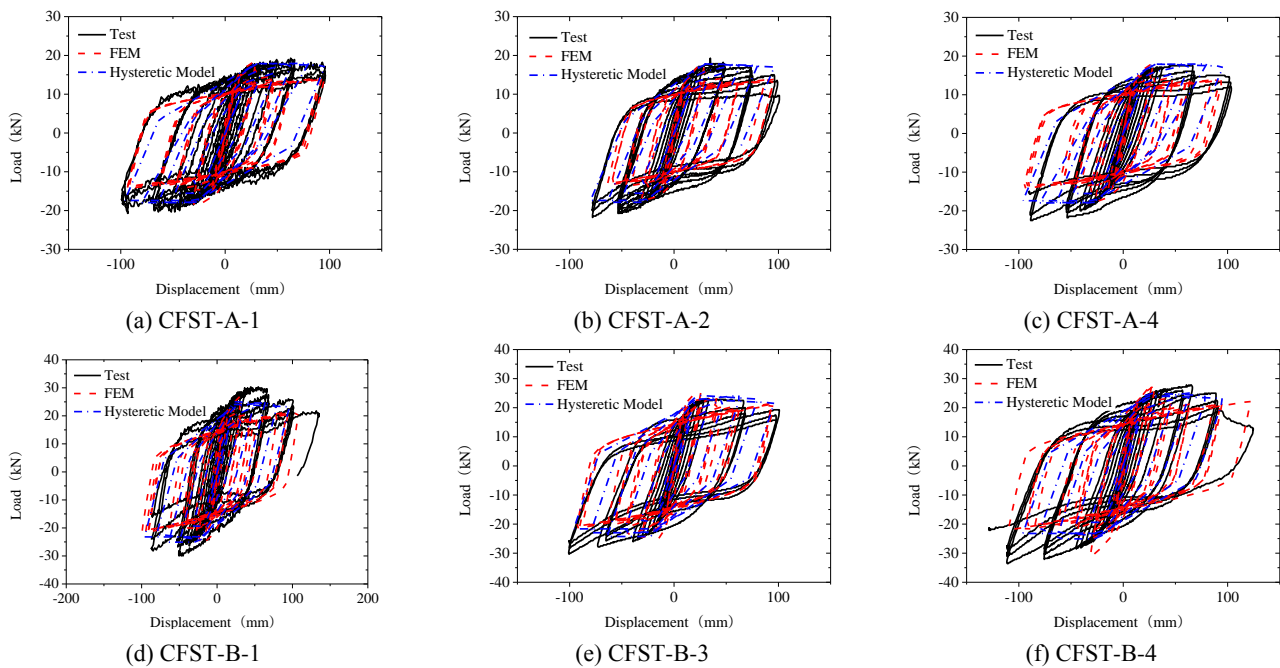(d) CFST-B-1      (e) CFST-B-3      (f) CFST-B-4

Fig. 6 Hysteresis curve

The calculation was carried out from the end of the elastic stage and stopped at the end of the loading phase. The specimen was unloaded by the elastic rigidity $K_a$ from Point 1 or Point 4 and then loaded in the reverse direction to Point 2 or Point 5. The ordinates of Point 2 and Point 5 were 0.2 times those of at Points 1 and 4. The strain-softening stage of 23 or 5D was reached with the continued reverse loading. Point 3 and D were both located on the extension of OA, the ordinate of which were the same as that of Point 1 (3) and Point 4 (D).

## 4. Specimen deformation and strain

### 4.1 Macro-damage state

There was no obvious change in the specimens at the initial stage because it was in the elastic loading stage. As the load and displacement increased, the specimens entered the elasto-plastic development stage. At this time, a slight barrelling occurred at the bottom of the specimens. The strain gradually reached the yield strain. With the further increase of the load and displacement, the barrelling became obvious, and the lateral and vertical cracks could be observed on the specimen. After loading, surface waves were formed at both sides of the specimens, and some specimens experienced lateral cracking or longitudinal cracking over various lengths. The pre-stressed steel cables were in good working condition during the test. The typical failure mode of the specimen is shown in Fig. 5. The location of maximum stresses in finite element models were basically similar to the location of cracks on the specimens. The FEM calculation results could reflect the trendy of destruction form.

### 4.2 Hysteresis curve

The hysteresis curve obtained by the FEM and hysteretic model agrees well with the experimental results, which can reflect the bearing capacity of the specimen

under horizontal cyclic load. The accuracy of FEM and hysteretic model was verified. The hysteresis curve of some components is shown in Fig. 6.

The hysteresis curves of specimens, in the initial stage, are basically coincident and linear. The initial elastic stiffness of the specimens is unchanged and no residual deformation can be observed. The specimen is in the state of elasticity and the hysteresis curve is a typical fusiform shape. Under load, the specimen gradually enters to the elasto-plastic working state. Residual deformation occurred in the specimen and displacement hysteresis is obvious. The displacement within the unit loading gradient is great, indicating that stiffness of the specimen degraded; but hysteresis curve remained full and LACFST had good energy dissipation performance. It can be seen from Figs. 6(a), (c), (d), and (f) that there is no significant difference between the hysteresis curves of the specimens with, or without, tunnels, and the energy dissipation performance is similar. The diameter of the reserved tunnel is small and it lies at the centre of the steel pipe and the existence of the tunnel has little influence on the inertia moment of the specimen, thus the mechanical behaviour of the specimen under the horizontal load is unaffected.

### 4.3 Skeleton curve

The P-Δ skeleton curve of the specimens is shown in Fig. 7. The skeleton curves of specimens at the initial loading were basically coincident, indicating that the specimens are at the stage of elasticity. Then the horizontal

thrust increases slowly when the loading displacement increases greatly, indicating that the specimen gradually enters the elastoplastic working stage. At the end of loading, the horizontal thrust gradually decreases with the loading displacement unchanged, and the specimen experiences significant stiffness degradation. The skeleton curves of the two groups of specimens decreases gradually at the later stage, which is mainly due to the restraining effects of the steel tube on the core concrete. The core concrete is in the three-way compression state and the compressive and deforming ability are improved to some extent. At the same time, the core concrete plays a certain supporting role on the steel pipe wall, avoiding or delaying the concave buckling of the steel pipe wall for better stability.

### 4.4 Strain analysis

#### 4.4.1 Steel pipe strain

The macroscopic failure modes of the specimens are similar: local buckling occurred at the bottom of the steel pipe, forming an obvious barrell wave. The local cracking can be observed in the barrel of some specimens. The strain data of the outer wall of the steel pipe indicates that the strain changes at measuring points in each specimen are similar. Therefore, the strain data from the front side, and hoop point, of CFST-B-4 are selected for analysis.

Measuring points 1# (3#) are closest to the bottom of the steel tube, so the strain during formation of the plastic hinge was recorded. As seen in Fig. 8(a), the strain at the bottom of the steel tube increased linearly with increasing load and
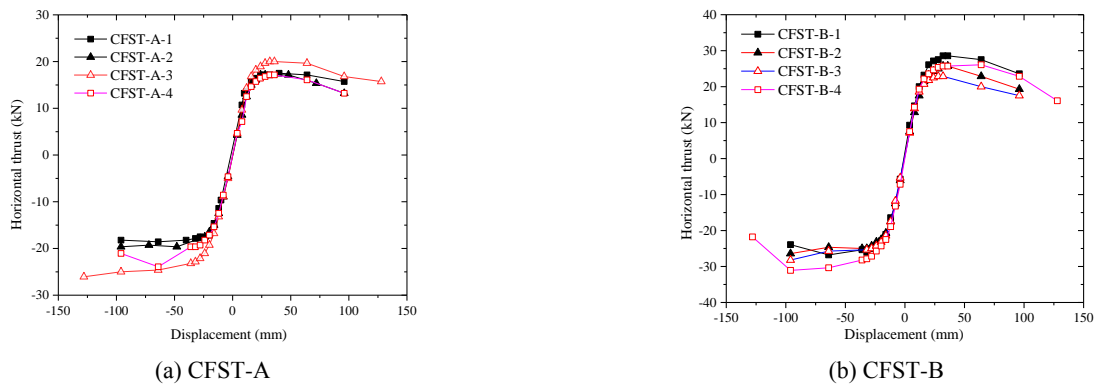


(a) CFST-A



(b) CFST-B

Fig. 7 Skeleton curve



(a) CFST-B-4 front side measurement point
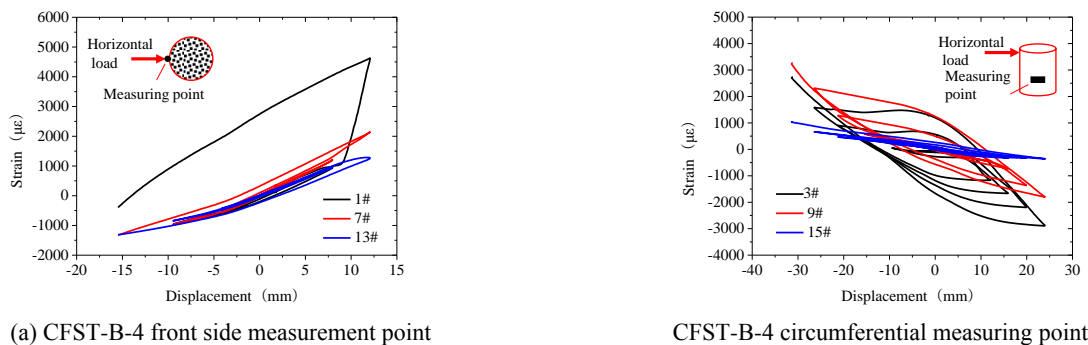


CFST-B-4 circumferential measuring point

Fig. 8 Steel pipe strain profiles

displacement, indicating that the steel tube was still in the elastic working stage. When the displacement increases to about 10 mm, the strain at the bottom of the steel pipe increases rapidly and the hysteresis loop area formed by the strain is also increasing. As the number of cycles increases, the hysteresis loop generated by the deformation of the steel pipe gradually moved upwards at the same displacement and load, indicating that irreversible plastic deformation occurred at bottom of the steel pipe, and that a plastic hinge has also formed.

The distances between measuring points 7# (9#), 13# (15#), and the bottom of the steel pipe were 80 mm and 180 mm, respectively. As seen in Fig. 8(a), the strain at 7# measuring point changes linearly during the loading, and did not enter the non-linear stage until later. This is because the barrel of the steel tube bottom is great and has influence on the measuring point 7#. The strain of the measuring point 13# changes linearly because it is far from the barrel and the rigidity of the steel tube is not affected. This also indicates that local buckling at the bottom results in the fracturing of the steel tube.

From Fig. 8(b), the strain at measuring point 15# changes almost linearly, which is similar to that at measuring point 13#, indicating that the steel tube exerted little restraining effect on the core concrete. The strain at measuring point 9# changes linearly at first and then non-linearly because the influence of the steel tube wall on the core concrete is gradually enhanced by the barrel at the bottom of the steel tube. The strain at measuring point 3#, located at the barrel, enters the non-linear stage first. The displacement-strain hysteresis curve is full and the area of the hysteresis loop gradually increases with the load, which shows that the restraining effect of the steel pipe on core concrete is gradually increasing and the steel tube words well with the core concrete.

### 4.4.2 Concrete strain

The thin copper sheet with uniaxial strain gauges were attached to the interior of the concrete to measure the strain in the core concrete during loading. The strains in CFST-A-4 and CFST-B-4 from displacements of -32 mm to +32 mm were selected for analysis (Fig. 9).

As seen in Fig. 9, at the initial stage of loading, the strain at the measuring point 20#, located 80 mm from the bottom of the specimen, is small and linear, indicating that the core concrete is elastic. With increased load and

displacement, the strain at measuring point 20 # increased slightly while the rate of increase is slow, indicating that a certain deformation occurs in the core concrete under external load. When the loading displacement reaches 32 mm, the maximum strains at measuring point 20# in CFST-A-4, CFST-B-4 were about 260 $\mu\varepsilon$ and 180 $\mu\varepsilon$, respectively, that is, the stress in the core concrete here is about 7.8 MPa and 5.4 MPa. The stress is much smaller than the compressive strength of the core concrete and the core concrete is elastic under the constraint of the steel pipe. The strain at measuring point 19#, located 20 mm from the bottom of the specimen, is small, indicating that the core concrete is elastic. With the increase of the loading displacement, the strain at measuring point 20 # increases rapidly. The strain at measuring point 19# increases rapidly as the load displacement increases. The maximum strain at point 19#, in CFST-A-4, is 7400 $\mu\varepsilon$, which exceeds the ultimate compressive strain of light aggregate concrete, indicating that the concrete has been crushed and destroyed. The steel tube also reaches the yield point. The external load is mainly carried by the steel pipe and the specimen gradually enters the failure stage.

## 5. Bearing performance analysis

### 5.1 Analysis of influencing factors

The accuracy of the FEM was verified by the comparison with the experimental results. Taking into account the limitations of the experiments, the parameters of the specimens were expanded by FEM to study the bearing capacity of LACFST under different influencing factors.

The FEMs were built based on light aggregate concrete with the strengths of CL20, CL30, CL40, and CL50, respectively, and the loading-displacement skeleton curve was obtained, as shown in Fig. 10. It can be seen that the ultimate bearing capacity of LACFST increases with the increasing strength of lightweight aggregate concrete: however, the ultimate deformation capacity of the LACFST, after the ultimate load was reached, is weakened. The bearing capacity decreases rapidly, and the ductility of the LACFST is reduced.

The skeleton curves of the LACFST with axial pressure ratios of 0, 0.2, 0.4, and 0.8 are compared in Fig. 11. It can
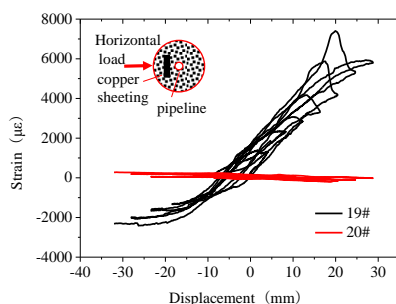


(a) Concrete internal measuring points of CFST-A-4
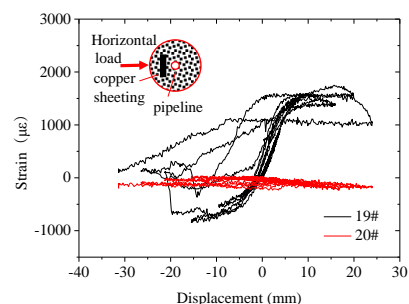
(b) Concrete internal measuring points of CFST-B-4

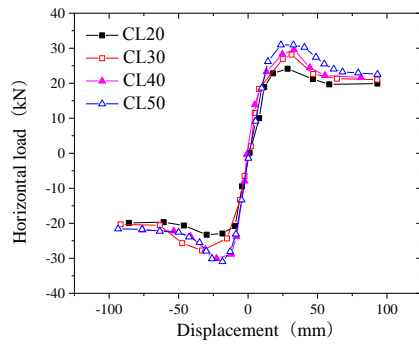Fig. 9 Concrete strain profiles

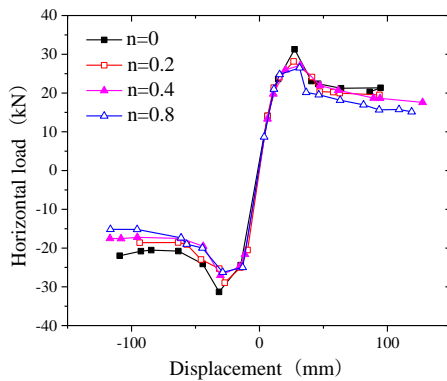Fig. 10 Skeleton curve of different lightweight aggregate
concrete members



Fig. 12 Skeleton curve of different diameter-thickness
ratio components



Fig. 11 Skeleton curve of different axial compression ratio
members



Fig. 13 Skeleton curve of different steel pipe strength
members

be seen that, in the elastic phase, the skeleton curves of the LACFST develops consistently, and the axial compression ratio has little effect on the skeleton curve. With increased loading displacement, the component enters the plastic working stage. As the axial compression ratio increases, the ultimate load of the LACFST decreases slightly and the ultimate displacement decreases. In the later stage of loading, the LACFST fails and the skeleton curve with the larger axial compression ratio is steeper and the ductility of the LACFST is continuously reduced.

The skeleton curves of LACFST with different diameter to thickness ratios are compared in Fig. 12. The outer diameter of each LACFST is 133 mm while the thicknesses of the steel tube are 3 mm, 5 mm, and 7 mm, respectively. It can be seen that the ratio of diameter to thickness affects the skeleton curve of the LACFST. As the diameter-to-thickness ratio decreases, the ultimate bearing capacity and ultimate deformation increase significantly. At the end of loading, the bearing capacity decreases slowly. When the ratio of diameter to thickness is small (at a wall thickness of 7 mm), there is no falling section in the skeleton curve, which indicates that the ductility of the component increases as the ratio of diameter to thickness decreases. As the thickness of the steel tube increases, the constraint on the core lightweight aggregate concrete increases. As the steel tube bears more load, under the action of the applied horizontal cyclic load, the core lightweight aggregate concrete had not yet reached the failure stage.
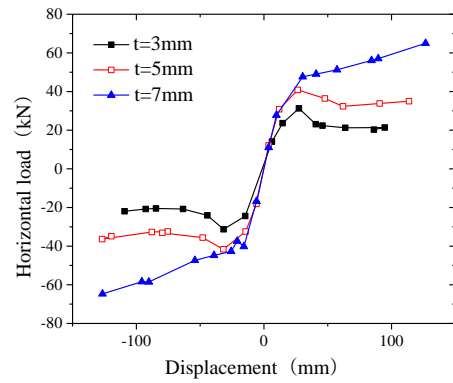
The skeleton curves of LACFST with different steel tube strengths are compared in Fig. 13. The steel tubes are made of steel of grade Q235, Q345, and Q390. In the early stage of loading, each LACFST is in its elastic working phase, and the load-displacement skeleton curve develops almost uniformly. As the displacement and load increase, the bearing capacity of the steel tube with the highest strength also increases significantly. After entering the destruction stage, there is no significant difference in the downward trend of each component, that is, the ductility of the components is similar.

### 5.2 Strength degradation and stiffness degradation

#### 5.2.1 Strength degradation
After the lightweight aggregate concrete filled steel tube yields, each cycle of displacement is loaded three times, which is used as an indicator of strength degradation. The strength degradation formula is as follows

$$\lambda = P_{i,j}/P_{i,1} \qquad (11)$$

Where, $P_{i,j}$ is the peak horizontal thrust load corresponding to the $j$ cycle at the loading $i$; $P_{i,j}$ is the peak horizontal thrust load corresponding to the first cycle of loading $i$.

The strength degradation of the perforated CFST-A and

CFST-B specimens is shown in Fig. 14: the abscissa represents the ratio of the target displacement to the yield displacement. The ordinate represents the strength degradation factor for the second and third displacement loading cycle. There is no significant difference between the intensity degradation curves of CFST-A-1 and CFST-A-4, CFST-B-1, and CFST-B-4, indicating that the prestressed tendons reserved at the core had no influence on the LACFST. In general, as the displacement increases, the strength curve of the test piece gradually falls. The larger the axial compression ratio, the more stable the strength coefficient of the test piece.
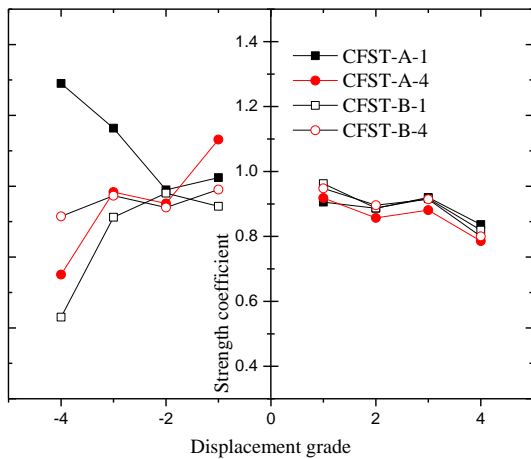
### 5.2.2 Stiffness degradation

Stiffness degradation is an important indicator reflecting the mechanical properties of structures or components in low-cycle cyclic load tests. The displacement of peak points increases with increasing numbers of loading cycles under the same peak horizontal load. The equivalent stiffness is used to represent the stiffness degradation of the specimen under low-cycle repeated loading. The equivalent stiffness

is calculated by the following formula

$$K_{hj} = \frac{\sum_{i=1}^{n} P_{j,i}}{\sum_{i=1}^{n} \Delta_{j,i}} \qquad (12)$$

Where, the $K_{hj}$ represents the stiffness at the cycle $j$; $P_{j,i}$ represents the peak horizontal thrust load corresponding to the $i$th cycle at load $j$; $\Delta_{j,i}$ represents the corresponding level of load $j$ and the displacement corresponding to meter No. 1 at cycle $i$; $n$ is the number of cycles. The equivalent stiffness curve of the test piece is shown in Fig. 15.

As seen in Fig. 15(a), at the same axial compression ratio, the stiffness degradation curves of the perforated and non-porous specimens are similar, indicating that the provision of the prestressed steel pipe at the centre of the components has little effect on the stiffness of the test piece. From Figs. 15(a) and (b), the stiffness degradation curves of the CFST-B specimens are located above those of the CFST-A specimens. The stiffness of the CFST-B during loading is greater than that of the CFST-A because the outer diameter and the hoop coefficient of the CFST-B are larger
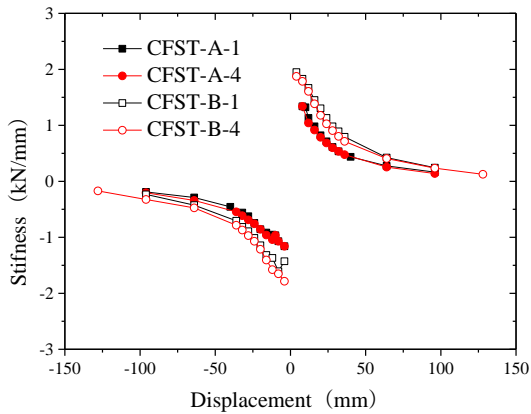


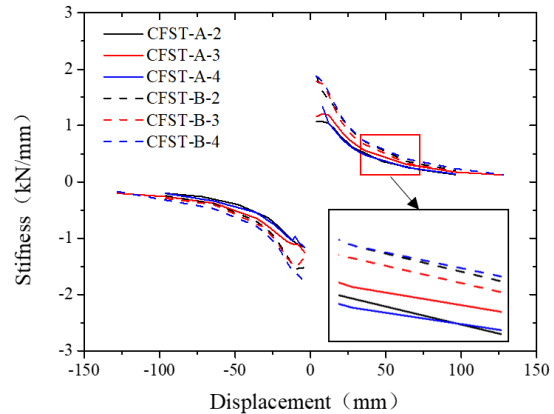(a) Strength degradation curve of perforated and non-porous specimens
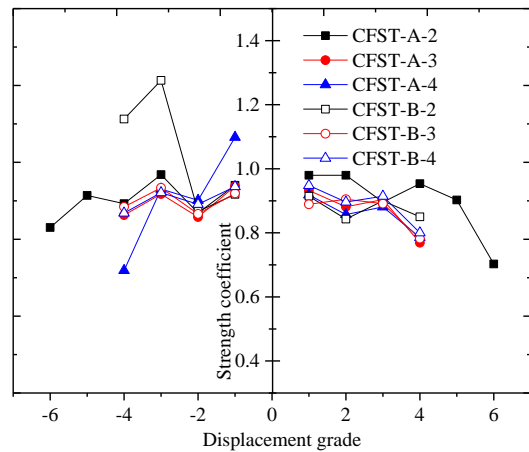
(b) Strength degradation curve of perforated specimens

Fig. 14 Intensity degradation curve comparison



(a) Stiffness degradation curve of perforated and non-porous specimens

(b) Stiffness degradation curve of perforated specimens

Fig. 15 Comparison of stiffness degradation curves

Table 3 Ductility coefficient of specimens

| Specimens | Yield point | | Peak point | | Destruction point | | $\mu = \Delta_u / \Delta_y$ |
|-----------|-------------|-----------|------------|-----------|-------------------|-----------|------------------------------|
| | $P_y$/ kN | $\Delta_y$/ mm | $P_m$/ kN | $\Delta_m$/ mm | $P_u$/ kN | $\Delta_u$/ mm | |
| CFST-A-1 | 14.93 | 16.94 | 19.58 | 68.33 | 14.81 | 95.81 | 6.42 |
| CFST-A-2 | 15.52 | 18.05 | 19.15 | 48.99 | 12.83 | 95.78 | 6.17 |
| CFST-A-3 | 21.59 | 20.94 | 24.38 | 80.34 | 20.85 | 126.81 | 7.21 |
| CFST-A-4 | 16.54 | 21.98 | 20.89 | 64.59 | 13.045 | 96.14 | 5.81 |
| CFST-B-1 | 22.43 | 20.25 | 29.37 | 62.47 | 17.87 | 96.91 | 4.32 |
| CFST-B-2 | 20.29 | 19.05 | 26.43 | 48.51 | 19.68 | 96.36 | 4.75 |
| CFST-B-3 | 21.09 | 16.94 | 25.82 | 48.31 | 20.84 | 95.86 | 4.55 |
| CFST-B-4 | 22.87 | 17.03 | 30.74 | 79.83 | 18.82 | 128.76 | 5.63 |

than those of the CFST-A. The steel pipe offers a stronger restraint to the core concrete. The converted cross-sectional area of CFST-B is therefore greater.

As seen in Fig. 15(b), the stiffness degradation curve of the test piece where the barrel portion is cracked is basically consistent with that of other test pieces, indicating that the local cracking of the barrel portion has no significant influence on the overall rigidity of the specimen. For the CFST-A, the stiffness degradation curve, at large axial compression ratio, is above than that with the smaller axial compression ratio. For CFST-B, the stiffness degradation curve, at a large axial compression ratio, is below than that with the smaller axial compression ratio. This is because the outer diameter of the CFST-A is smaller. Although the larger axial compression ratio is beneficial to the triaxial effect restraining the core concrete, the larger the axial compression ratio,, the more likely the localised buckling of the steel pipe wall around transverse cracks and longitudinal cracks in CFST-A-2 and CFST-A-3, therefore, the greater the axial compression ratio, the smaller the stiffness of the specimen. The outer diameter of the steel pipe of the CFST-B test piece is large, and the steel pipe wall is not prone to local instability and the core concrete is in the triaxial state of stress when the axial pressure is relatively large. For example, CFST-B-4 produces lateral cracking in the barrel portion, as does CFST-B-2. CFST-B-3 exhibits barrelling only, thus, the stiffness of the member increases as the axial compression ratio increases.

## 6. Ductility and energy consumption

### 6.1 Ductility factor

The energy equivalent method $\mu = \Delta u / \Delta y$ is used to calculate the ductility coefficient of the specimen (Jeddi *et al.* 2017). Where, $\Delta u$ is the ultimate displacement of the specimen and the corresponding displacement is taken when the peak load drops to 85% of its peak; $\Delta y$ is the yield displacement. The calculated ductility coefficients and eigenvalues are listed in Table 3.

As seen in Table 3, the ductility coefficients of the specimen are all greater than 4, indicating that the steel column lightweight aggregate concrete columns have good seismic deformation resistance. The ductility coefficients of
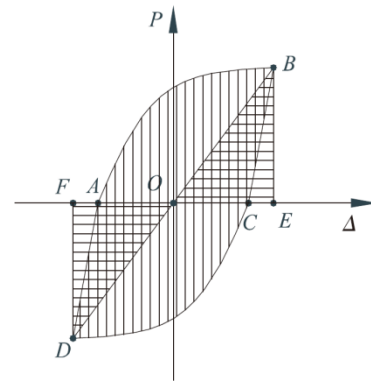
Fig. 16 Calculation of the equivalent viscous damping coefficient calculation
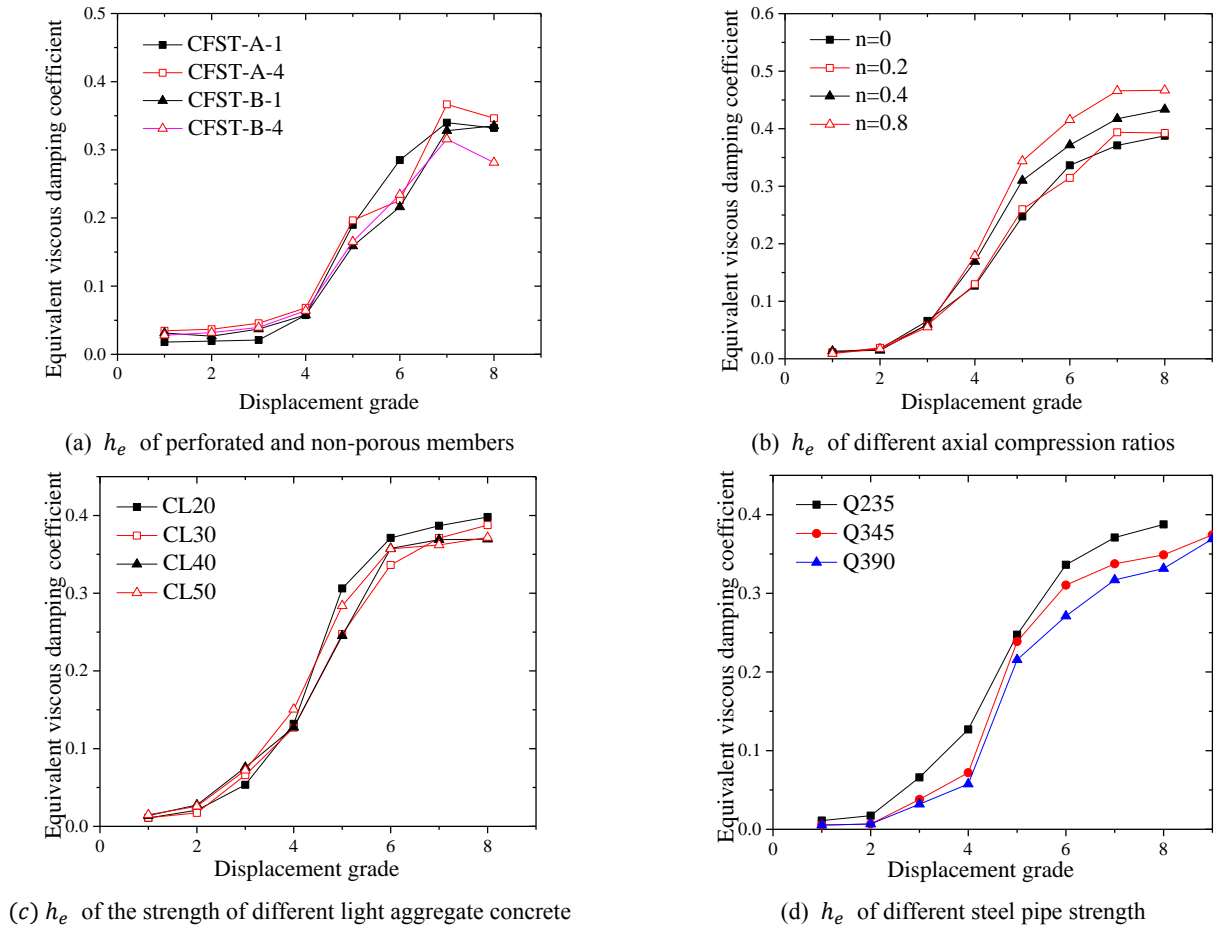
the perforated and non-porous specimens are similar, indicating that the prestressed tendon pipe has no effect on the ductility of the specimen. The ductility coefficient of CFST-A specimens is greater than that of CFST-B specimens, indicating that the larger the outer diameter of the steel tube, the lower the ductility of the specimen. This is because the outer diameter of the steel tube is smaller and the steel content of the cross section is larger. Otherwise, the steel has an excellent plastic deformation performance and the plastic deformation resistance of the concrete is poor. The ductility coefficient of the specimen with the smaller outer diameter is higher, and the ductility coefficients of the test pieces in each group are similar, indicating that the axial pressure ratio has little effect on the ductility coefficient.

### 6.2 Equivalent viscous damping coefficient

The equivalent viscous damping coefficient $h_e$ is used to evaluate the energy dissipation capacity of the test piece. The calculation formula (Wang *et al.* 2018) is as follows

$$h_e = \frac{1}{2\pi} \frac{S_{ABCD}}{S_{\Delta OBE} + S_{\Delta OFD}} \tag{13}$$

Where, the $S_{ABCD}$ represents the hysteresis loop area, $S_{\Delta OBE}$ and $S_{\Delta OFD}$ represent the triangle area corresponding to the peak point of the hysteresis loop (Fig. 16). The equivalent viscous damping coefficient at each cyclic

(a) $h_e$ of perforated and non-porous members



(b) $h_e$ of different axial compression ratios



(c) $h_e$ of the strength of different light aggregate concrete



(d) $h_e$ of different steel pipe strength

Fig. 17 $h_e$ curves

displacement of each test piece is calculated (Fig. 17).

The equivalent viscous damping coefficient of each specimen increases with the load, and finally stabilises. The test pieces are stable between 0.3 and 0.4, however, the equivalent viscous damping coefficient of ordinary reinforced concrete columns is about 0.1 to 0.2, so the steel lightweight aggregate concrete columns have better energy dissipation capacity. From Fig. 17(a), the comparison of the equivalent damping coefficients of the two groups of holes and non-pores shows that the existence of the prestressed tunnels has little effect on the equivalent viscous damping coefficient. The prestressed tube has little effect on the energy absorbed by the test piece. Fig. 17(b) shows the variation of the equivalent viscous damping coefficient of specimens at different axial compression ratios. As the axial compression ratio increases, the equivalent viscous damping coefficient of each specimen increases continuously because the specimen with the larger axial compression ratio will undergo plastic deformation earlier and the energy absorption capacity will increase accordingly. It can be seen from Fig. 17(c) that the influence of the strength of the lightweight aggregate concrete on the equivalent damping coefficient is not significant, and the test pieces can reach a value of 0.35 or more, showing good energy dissipation performance. Fig. 17(d) shows that, at the same load and displacement, the equivalent viscous damping coefficient decreases with

the increase of the strength of the steel pipe since the specimen with the lower strength of the steel pipe enters the yield phase earlier under the same displacement and load. The larger deformation increases the energy absorption of the specimen.

## 7. Conclusions

The horizontal cyclic load test and finite element analysis are carried out on the LACFST, and the following conclusions obtained:

(1) The experimental results of the steel tube and concrete show that the core concrete of the LACFST is crushed first under the horizontal cyclic load. The load is then carried by the steel tube until the ultimate strength of the steel tube is reached. A barrel forms on the tube wall and cracks, of various lengths, are observed. The axial force can be applied by a prestress and the prestressed tunnel exerts no influence on the mechanical performance of the LACFST.

(2) The test results show significant hysteresis in the LACFST. The ductility coefficient of the specimen is greater than 4.5, and the equivalent viscous damping coefficient is between 0.25 and 0.4, which

is about two times that of an ordinary CFST. The LACFST offers good energy dissipation performance.

(3) The calculated results arising from use of the proposed constitutive model of an LACFST agree with those from experiments, and can thus be applied to the FEM analysis of the LACFST. The proposed hysteretic model reflects each stage of LACFST behaviour under horizontal cyclic load and accurate hysteresis curves can be obtained.

(4) The experiments and FEM results show that the bearing capacity and ductility of the member increased with increasing thickness of the steel tube. The greater the strength of the steel tube and lightweight aggregate concrete, the higher the bearing capacity of the specimen, while the ductility, and energy dissipation performance, of the member decrease slightly. The bearing capacity and ductility of the specimen decrease slightly while the energy consumption performance increases as the axial compression ratio increases.

## Acknowledgments

## References

Arivalagan, S. and Kandasamy, S. (2010), "Test of void-filled SHS beams under cyclic loading", *J. Reinf. Plast. Compos.*, **29**(10), 1534-1544. https://doi.org/10.1177/0731684408100896

Duarte, A.P.C., Silva, B.A., Silvestre, N., De Brito, J., Júlio, E. and Castro, J.M. (2016), "Experimental study on short rubberized concrete-filled steel tubes under cyclic loading", *Compos. Struct.*, **136**(2), 394-404. https://doi.org/10.1016/j.compstruct.2015.10.015

Esfandyary, R., Razzaghi, M.S., Eslami, A. and Branch, T. (2015), "A parametric investigation on the hysteretic behaviour of CFT column to steel beam connections", *Struct. Eng. Mech., Int. J.*, **55**(1), 205-228. https://doi.org/10.12989/sem.2015.55.1.205

Fu, Z.Q., Wang, Q.D., Wang, Y.X. and Ji, B.H. (2018), "Bending performance of lightweight aggregate concrete-filled steel tube composite beam", *KSCE J. Civil Eng.*, **22**(10), 1-9. https://doi.org/10.1007/s12205-018-0660-z

Ge, H.B. and Usami, T. (1996), "Cyclic tests of concrete-filled steel box columns", *J. Struct. Eng.*, **122**(10), 1169-1177. https://doi.org/10.1061/(ASCE)0733-9445(1996)122:10(1169)

Ghannam, S., Jawad, Y.A. and Hunaiti, Y. (2004), "Failure of lightweight aggregate concrete-filled steel tubular columns", *Steel Compos. Struct., Int. J.*, **4**(1), 1-8. https://doi.org/10.12989/scs.2004.4.1.001

Guo, Z.H. (1982), "Experimental study on the stress-strain curve of concrete", *J. Build. Struct.*, **3**(1), 1-12. [In Chinese] https://doi.org/10.3151/jact.2.395

Hajjar, J.F. (2000), "Concrete-filled steel tube columns under earthquake loads", *Progress Struct. Eng. Mater.*, **2**(1), 72-81.

https://doi.org/10.1002/(SICI)1528-2716(200001/03)2:1<72::AID-PSE9>3.0.CO;2-E

Han, L.H. and Yang, Y.F. (2005), "Cyclic performance of concrete-filled steel CHS columns under flexural loading", *J. Constr. Steel Res.*, **61**(4), 423-452. https://doi.org/10.1016/j.jcsr.2004.10.004

Inai, E., Mukai, A., Kai, M., Tokinoya, H., Fukumoto, T. and Mori, K. (2004), "Behavior of concrete-filled steel tube beam columns", *J. Struct. Eng.*, **130**(2), 189-202. https://doi.org/10.1061/(ASCE)0733-9445(2004)130:2(189)

Jeddi, M.Z., Sulong, N.R. and Khanouki, M.A. (2017), "Seismic performance of a new through rib stiffener beam connection to concrete-filled steel tubular columns: an experimental study", *Eng. Struct.*, **131**(1), 477-491. https://doi.org/10.1016/j.engstruct.2016.10.038

Ji, B., Fu, Z., Qu, T. and Wang, M. (2013), "Stability behavior of lightweight aggregate concrete filled steel tubular columns under axial compression", *Adv. Steel Constr.*, **9**(1), 1-13.

Khanouki, M.A., Sulong, N.R., Shariati, M. and Tahir, M.M. (2016), "Investigation of through beam connection to concrete filled circular steel tube (CFCST) column", *J. Constr. Steel Res.*, **121**(6), 144-162. https://doi.org/10.1016/j.jcsr.2016.01.002

Kim, D.H., Lee, C.H., Ju, Y.K. and Kim, S.D. (2015), "Subassemblage test of buckling-restrained braces with H-shaped steel core", *Struct. Des. Tall Special Build.*, **24**(4), 243-256. https://doi.org/10.1002/tal.1164

Krishan, A.L., Troshkina, E.A. and Chernyshova, E.P. (2016), "Efficient design of concrete filled steel tube columns", *Proceedings of the 2nd International Conference on Industrial Engineering*, Chelyabinsk, Russia, May.

Lee, H.J., Park, H.G., Park, S.S., Kim, S.B. and Choi, I.R. (2015), "Cyclic loading test for exterior beam–column joints of CEFT columns", *J. Struct. Eng.*, **142**(2), 04015147. https://doi.org/10.1061/(ASCE)ST.1943-541X.0001401

Liu, Y.B. (2013) "Study on hysteretic behavior of defective concrete filled steel tubular members", Master's Dissertation; Fuzhou University, Fuzhou, China. [In Chinese]

Roeder, C.W., Stephens, M.T. and Lehman, D.E. (2018), "Concrete filled steel tubes for bridge pier and foundation construction", *Int. J. Steel Struct.*, **18**(1), 39-49. https://doi.org/10.1007/s13296-018-0304-7

Samani, A.K. and Attard, M.M. (2012), "A stress–strain model for uniaxial and confined concrete under compression", *Eng. Struct.*, **41**(8), 335-349. https://doi.org/10.1016/j.engstruct.2012.03.027

Skalomenos, K.A., Hatzigeorgiou, G.D. and Beskos, D.E. (2015), "Modeling level selection for seismic analysis of concrete-filled steel tube/moment-resisting frames by using fragility curves", *Earthq. Eng. Struct. Dyn.*, **44**(2), 199-220. https://doi.org/10.1002/eqe.2465

Subramoni, P.T. and Saratha, J.P. (2018), "Behaviour of Beam-Column Subjected to Reversed Lateral Loading", *KSCE J. Civil Eng.*, **22**(7), 2464-2468. https://doi.org/10.1007/s12205-017-2023-6

Tort, C. and Hajjar, J.F. (2009), "Mixed finite-element modeling of rectangular concrete-filled steel tube members and frames under static and dynamic loads", *J. Struct. Eng.*, **136**(6), 654-664. https://doi.org/10.1061/(ASCE)ST.1943-541X.0000158

Varma, A.H., Ricles, J.M. and Sause, R. (2000), "Seismic behavior, analysis, and design of high strength square concrete filled steel tube (CFT) columns", Doctoral Dissertation; Lehigh University, PA, USA.

Wang, Y.H., Lu, G.B. and Zhou, X.H. (2018), "Experimental study of the cyclic behavior of concrete-filled double skin steel tube columns subjected to pure torsion", *Thin-Wall. Struct.*, **122**(6), 425-438. https://doi.org/10.1016/j.tws.2017.10.034

Yu, X., Tao, Z. and Song, T.Y. (2016), "Effect of different types of

aggregates on the performance of concrete-filled steel tubular stub columns", *Mater. Struct.*, **49**(9), 3591-3605. https://doi.org/10.1617/s11527-015-0742-z

*CC*